Author/s:
Barras, V;Simmonds, I

Title:
Observation and modeling of stable water isotopes as diagnostics of rainfall dynamics over southeastern Australia

Date:
2009-01-01

Citation:
Barras, V. & Simmonds, I. (2009). Observation and modeling of stable water isotopes as diagnostics of rainfall dynamics over southeastern Australia. Journal of Geophysical Research Atmospheres, 114 (23), https://doi.org/10.1029/2009JD012132.

Publication Status:
Published

Persistent Link:
https://hdl.handle.net/11343/32755

Observation and modeling of stable water isotopes as diagnostics of rainfall dynamics over southeastern Australia

Vaughan Barras[1] and Ian Simmonds[2]

Received 29 March 2009; revised 4 August 2009; accepted 4 September 2009; published 9 December 2009.

[1] A unified approach of observation and modeling was applied to the investigation of three circulation types that typically bring rain to southeastern Australia. Observations from the Melbourne University Network of Isotopes in Precipitation of high-resolution variations in the ratios of ^{18}O and ^{2}H were collected for (1) mixed frontal, (2) convective, and (3) stratiform precipitation events. Isotopic content of precipitation varied over both high and low frequencies because of influences from local variations in rain intensity and rainout by large-scale precipitation. Deuterium excess showed a weak relationship with rainfall amount on intraevent time scales but was stronger under convective rainfall conditions. As a supplement to the observations, a version of the National Center for Atmospheric Research Community Atmosphere Model running an isotope hydrology scheme simulated the mixed frontal and stratiform events by nudging with reanalyses. The simulations represented well the evolution of vapor profiles of ^{18}O and deuterium excess. Trajectories for the mixed frontal case illustrated the structure of the vapor profiles, revealing a convergence of air masses from different source regions. Deuterium excess in precipitation was represented less accurately by the model, indicating a possible shortcoming in the parameterization of postcondensation processes in the general circulation model. By combining observations and modeling in this way, detail of the structure and history of the events was provided that would be unavailable from the sampling of precipitation alone.

Citation: Barras, V., and I. Simmonds (2009), Observation and modeling of stable water isotopes as diagnostics of rainfall dynamics over southeastern Australia, *J. Geophys. Res.*, *114*, D23308, doi:10.1029/2009JD012132.

1. Introduction

[2] Many of the processes associated with the fractionation of the stable water isotopes $H_2^{18}O$ and $^1H^2HO$ from $H_2^{16}O$ during changes of phase throughout the hydrological cycle are reasonably well understood. However, the application of stable water isotopes as tracers of moisture is often hindered by the coarse resolution of observational data. Measurements of $^{18}O/^{16}O$ and $^{2}H/^{1}H$ ratios of precipitation have proven useful as diagnostics over a range of scales in surveys of the spatial variability of precipitation [*Dansgaard*, 1964; *Salati et al.*, 1979; *Rozanski et al.*, 1993; *Celle-Jeanton et al.*, 2001; *Friedman et al.*, 2002b; *Longinelli and Selmo*, 2003; *Argiriou and Lykoudis*, 2006; *Lykoudis and Argiriou*, 2007] and trajectory analysis of air mass history [*Lawrence et al.*, 1982; *Gedzelman and Lawrence*, 1982; *Rindsberger et al.*, 1990; *Friedman et al.*, 2002a; *Burnett et al.*, 2004; *Peng et al.*, 2004; *Barras and Simmonds*, 2008; *Pfahl and Wernli*, 2008], revealing much about the structure and evolution of rain-bearing weather systems over particular regions. Similarly, intensive observation periods (IOPs) of isotopes in precipitation have been valuable in quantifying the effects of vapor recycling, convection, cloud top height and droplet reevaporation [*Dansgaard*, 1953; *Miyake et al.*, 1968; *Gedzelman and Lawrence*, 1982, 1990; *Pionke and DeWalle*, 1992; *Risi et al.*, 2008; *Risi et al.*, 2009] and have also been useful in the development of isotopic models of varying complexity [*Lee and Fung*, 2008; *Bony et al.*, 2008]. This study takes a unified approach, combining observations of isotopic variability collected over a number of IOPs with simulations of the events using an isotope-enabled general circulation model (GCM) to identify the important effects upon isotopes in precipitation in southeast Australia.

[3] The observational component of this study involved the establishment of the Melbourne University Network of Isotopes in Precipitation (MUNIP). MUNIP was devised to sample rainwater simultaneously at a number of sites across the city and surrounding suburbs of Melbourne, Australia. Collections were made during the occurrence of typical key precipitation types during the summer and winter seasons between 2003 and 2005. MUNIP is unique in that it is the first time that isotope data have been collected in this way over such a broad area and on such short time scales in Australia. From the early observational studies of *Dansgaard* [1953] and *Miyake et al.* [1968], it became apparent that there were distinctive temporal behaviors in the ratios

[1]Centre for Australian Weather and Climate Research, Bureau of Meteorology, Melbourne, Victoria, Australia.
[2]School of Earth Sciences, University of Melbourne, Melbourne, Victoria, Australia.

0148-0227/09/2009JD012132

of ^{18}O during the passage of individual rain events. In a series of observational studies, *Miyake et al.* [1968] noted particularly sharp decreases in the ^{18}O content of frontal precipitation. Their observations also revealed an inverse correlation between precipitation intensity and ^{18}O content under prevailing convective conditions during frontal rainfall events. Miyake et al. attributed this to the arrival of moisture from the cooler and hence more isotopically depleted environment aloft. More recently, *Celle-Jeanton et al.* [2004] identified characteristic isotopic trends in the most common midlatitude rainfall "types" over southern France, finding these to be similar to those described by *Rindsberger et al.* [1990] during rain events sampled over Israel. Both found that stratiform rainfall exhibited a gradual decrease in isotope ratio over the duration of the event and attributed this to the preferential condensation ("rainout") of the heavier isotopes over time. Convective rainfall events were characterized by sharp L- or W-shaped patterns in the evolution of the isotopes as cells of convection drew moisture from the colder and hence more isotopically depleted environment aloft.

[4] In addition to measurements of the ratios $^{18}O/^{16}O$ and $^{2}H/^{1}H$, the secondary parameter, the "deuterium excess" (d) may be calculated such that $d = \delta^2H - 8\delta^{18}O$ [*Dansgaard*, 1964], where $\delta = [(R/R_{std}) - 1)] \times 1000$ and R is the ratio $X_i/X_i/X$, where X_i is the abundance of the isotopic form of X and R_{std} is the isotope ratio of a known reference standard. Evaporative effects upon moisture may either increase or decrease its d value away from its equilibrium value of 10‰. Departures from this value are regarded as an indication of the extent of nonequilibrium processes influencing the moisture during its history. Increases in deuterium excess may arise from the mixing of air masses or the recycling of evaporated moisture by the formation of a secondary condensate. This can be used to identify moisture from particular sources such as lakes or evapotranspiration from forest canopies [*Gonfiantini*, 1986; *Martinelli et al.*, 1996; *Henderson-Sellers et al.*, 2004]. Conversely, rapid evaporation, which most often occurs during the fall of rain droplets beneath the cloud base, has the effect of reducing the deuterium excess value of the residual water of the droplet because of the change in the rate of molecular exchange of ^{18}O relative to ^{2}H under nonequilibrium conditions. The extent of this change depends on droplet size, the fall distance, and the ambient vapor content [*Bolin*, 1958; *Jouzel*, 1975; *Stewart*, 1975]. For large-scale applications it is widely accepted that the deuterium excess of moisture within an air mass is set primarily during evaporation at the moisture origin [*Craig and Gordon*, 1965; *Merlivat and Jouzel*, 1979; *Pfahl and Wernli*, 2008], making d a valuable indicator of climatic changes of the past [*Jouzel et al.*, 1982; *Vimeux et al.*, 1999; *Masson-Delmotte et al.*, 2005]. However, when considered over very short time scales, such as the duration of an individual storm, the sensitivity of deuterium excess to rates of droplet formation and evaporation can significantly influence the measured value in precipitation [*Jouzel and Merlivat*, 1984; *Jacob and Sonntag*, 1991; *Liotta et al.*, 2006; *Peng et al.*, 2007].

[5] Increasingly, computer simulations have provided a more quantitative approach to the study of particular fractionation effects upon isotope variability [*Helsen et al.*, 2006; *Angert et al.*, 2008; *Lee and Fung*, 2008; *Masson-Delmotte et al.*, 2008; *Risi et al.*, 2008; *Bony et al.*, 2008; *Noone and Sturm*, 2009]. Attempts have been made at reconstructing isotopic exchange along moisture transport pathways using combinations of reanalyses and averaged isotope fields from GCMs [*Helsen et al.*, 2006; *Angert et al.*, 2008; *Sodemann et al.*, 2008a]. *Pfahl and Wernli* [2008] extended the trajectory method of *Sodemann et al.* [2008b] to identify oceanic moisture source regions over the eastern Mediterranean, finding a strong correlation between deuterium excess in water vapor and the near-surface relative humidity at the source location. Over the years, a number of GCMs have been adapted to include isotope fractionation in their hydrological cycles [*Joussaume et al.*, 1984; *Hoffmann et al.*, 1998; *Noone and Simmonds*, 2002; *Lee et al.*, 2007; *Tindall et al.*, 2009], providing valuable insights into moisture transport studies and paleoclimate reconstructions in particular [*Jouzel et al.*, 1997]. *Noone* [2006] developed a methodology to periodically impose dynamical constraints from reanalysis data upon the National Center for Atmospheric Research (NCAR) Community Atmosphere Model Version 3 (CAM3) [*Collins et al.*, 2006] with an isotope hydrology scheme (described in section 3.3) allowing isotope fractionation to freely evolve driven by the nudged dynamics. In this way, global isotope fields were able to be constructed that were consistent with the synoptic circulation and could be directly compared to case study observations. More recent work using this approach has been done by *Yoshimura et al.* [2008].

[6] We here use a unified approach of observation, modeling, and trajectory analysis in an investigation of isotope variability during the passage of weather systems that commonly bring rainfall to southeastern Australia. The intention of this is twofold. The primary aim is to examine the temporal evolution of stable isotope ratios during the passage of individual rain events at a number of sites across greater Melbourne. A secondary aim is to apply "dynamically constrained" isotope modeling to these events using a version of NCAR CAM3 to evaluate model performance and potentially extend the data coverage for the events. Section 2 describes the study region and typical summer and winter circulation patterns affecting the region. Section 3 introduces the methodology of the MUNIP data collection, each case study, and the CAM3 isotope simulations. Section 4 presents the observations and model results. Section 5 discusses some key findings from the observation and modeling studies, and section 6 contains some concluding remarks.

2. Location and Climate Summary

[7] Melbourne (37.8°S, 145.0°E) is situated in southeastern Australia on the northern and eastern shores of Port Phillip Bay, a large but shallow body of water covering approximately 1930 km^2 (inset in Figure 1). To the north of the city lies the western extension of the Great Dividing Range rising to between 800 and 1000 m to the northwest and up to 1250 m to the northeast. Both have an important influence upon the distribution of rainfall across the bay area. The mountain ranges cast a rain shadow across the suburbs to the west and north of the city under northwesterlies, and there is an increase in moisture loading of low

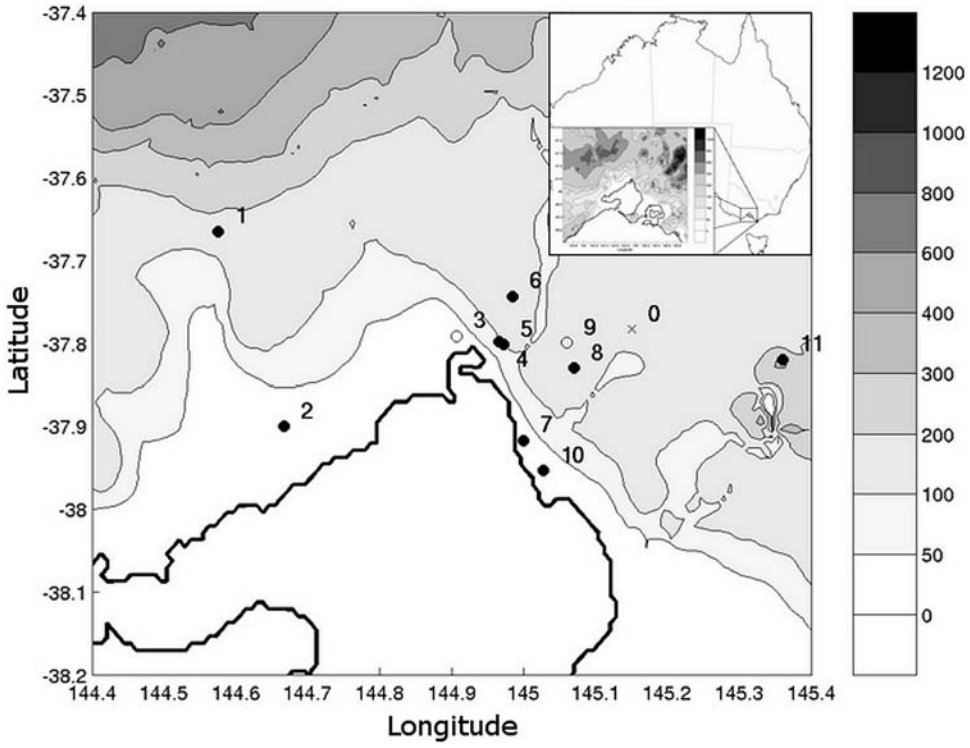

Figure 1. Location of Melbourne University Network of Isotopes in Precipitation (MUNIP) sites around Melbourne: 0, Doncaster (test site); 1, Melton; 2, Werribee; 3, Ascot Vale; 4, Melbourne University (Earth sciences); 5, Carlton (Queen's College); 6, Preston; 7, Brighton (test site); 8, Camberwell; 9, Canterbury; 10, Hampton East; 11, Kalorama. Topographic elevation contours are shown in meters; open circles indicate sites that were not used after the first case study measurement. Inset shows location of study region in Australia.

tropospheric air under southwesterly airflow, manifest in an almost threefold increase in annual rainfall along the west-east transect across the city.

[8] The summertime synoptic circulation over southeast Australia commonly features anticyclones positioned over the waters to the south of the Great Australian Bight and the Tasman Sea [*Fandry and Leslie*, 1984; *Jones and Simmonds*, 1993, 1994; *Simmonds and Keay*, 2000]. When the ridge between these is strong, humid air is drawn from the subtropics and the Tasman Sea under an easterly or northeasterly airflow, which can persist for several days. This pattern weakens the northward penetration of midlatitude frontal systems and establishes conditions conducive to the development of local afternoon and evening thunderstorms.

[9] The winter circulation in Melbourne is dominated by the regular passage of frontal systems in a prevailing west to southwesterly airstream. Stratiform rainfall from continental cloud bands account for about 35%–40% of cool season rainfall over southeastern Australia [*Wright*, 1997]. These are often followed by periods of convective showers as the wind backs to the southwest following the passage of the front.

3. Method

3.1. MUNIP Data Collection

[10] MUNIP consists of a number of rainwater sampling sites located around greater Melbourne. The sites vary in altitude, proximity to Port Phillip Bay, and topographical aspect and orientation, spanning approximately 100 km west to east (Figure 1). Sites to the north and west of the city (Melton, Werribee, Ascot Vale, Carlton, Earthsci, and Preston) lie on a relatively flat plain, whereas Camberwell and Canterbury are situated on the low undulating hills to the east of the city. The Hampton East site is relatively flat but has an exposure to the bay, whereas the Kalorama site is near the top of Mount Dandenong at an elevation of 460 m. At each of the MUNIP sites, rainfall was sampled manually from a rain gauge. Rainwater samples were removed at half-hourly intervals and immediately transferred to a rubber-sealed McCartney glass vial. Samples were stored in the vials for no longer than 3 months before analysis, and care was taken not to expose them to the air or extremes in temperature. Analyses were performed for abundances of ^{18}O and ^{2}H at the Department of Geosciences at Monash University in Melbourne. Values of ^{18}O were measured via equilibration with He-CO_2 at 32°C for 24–48 h in a Finnigan MAT Gas Bench and analyzed under continuous flow. Samples were analyzed for ^{2}H via reaction with Cr at 850°C using an automated Finnigan MAT H/Device. Both were measured relative to internal standards calibrated to International Atomic Energy Agency (IAEA) Vienna standard mean ocean water (VSMOW), Greenland Ice Sheet Precipitation (GISP), and standard light Arctic precipitation (SLAP), normalized following *Coplen* [1988] and reported in δ notation. With some MUNIP rainfall samples being of a small quantity, multiple sample measurements were not

always obtainable; however, where multiple analyses were performed, the precision of the measurements was ±0.3‰ for $\delta^{18}O$ and ±4‰ for $\delta^{2}H$, with an error of ±5‰ in subsequent calculations of deuterium excess.

3.2. Case Studies Typical of Key Rainfall Events

[11] The case studies targeted by MUNIP during 2004–2005 were representative of the characteristic rainfall types occurring in Melbourne as described in section 2. The events were classified as mixed frontal (9 June 2004), convective (6 December 2004), and frontal stratiform (11 June 2005). Figure 2 shows the synoptic charts and the MUNIP observations of rainfall for each of the case studies.

[12] The first case study is described as mixed frontal in the sense that both stratiform and convective rainfall occurred during the event. As a cold front passed across southeastern Australia, a mesoscale low-pressure system developed over Bass Strait (Figure 2a) under conditions favorable for cyclogenesis with upper divergence present from a diffluent upper trough and jet entrance region at 250 hPa, important precursors for severe convection in southern Australia [*Hanstrum et al.*, 2002]. Rainfall during this event occurred over two distinct periods. The first period (MF-1) was a prefrontal stratiform rainband that passed across the city between 0900 and 1600 local time (UTC+10). Rainfall was widespread and continuous during this period and simultaneous half-hourly samples were able to be obtained at five of the MUNIP sites (Figure 2b). The lowest rainfall amounts were recorded at the Preston and Melton sites to the north and west of the city, respectively. The remaining sites recorded several periods of peak rainfall intensity, first measured in Carlton followed by Canterbury and Hampton East as the convective cells embedded within the cloud band tracked from the northwest to the southeast. The second period of rain (MF-2) occurred between 2000 and 2300 and featured intense convective rainfall across the city causing local flash flooding and severe localized wind damage in the suburbs to the east of the bay. The atmospheric sounding prior to the event exhibited a potentially unstable air column above 850 hPa with a precipitable water value of 25.3 mm. Werribee recorded the greatest half-hourly rainfall (11.0 mm) at 2000, with relatively large totals also measured at the Earthsci and Camberwell locations. By contrast, the Ascot Vale and Preston sites received comparatively little rainfall, indicating the localized nature of the storm system.

[13] The second event measured rain samples from an outbreak of afternoon storms during the evening of 6 December 2004. During this period, the synoptic circulation over southeastern Australia was dominated by a large and deep pressure trough extending across the center of the continent that drew a very warm and humid northeasterly airflow over much of Victoria (Figure 2c). Large thunderstorms developed near the mountain ranges to the north of Melbourne during the afternoon and gradually moved southward over the city by evening. The IOP was short for this event, but representative samples were obtained, partly resembling the MF-2 phase of the mixed frontal event with an initial pulse of intense rainfall followed by a period of lighter showers (Figure 2d).

[14] The third and final measurement campaign sampled rain falling from a large continental cloud band that brought the first substantial amount of rain to Melbourne following a particularly dry autumn period. The cloud band was associated with the first of a series of cold fronts passing over southern Australia extending from a large and slow-moving parent cyclone over the Southern Ocean (Figure 2e). As with the first case study, measurements from this event were divided into two separate periods: scattered prefrontal rainbands (denoted S-1) from 1500 until 0500 and continuous moderate rain (S-2) from 0500 until 1130. MUNIP sampled rain from a prefrontal trough that passed over the city during the evening of 10 June resulted in areas of patchy, light rainfall (Figure 2f). By 0100 local time, the frontal rainband had begun to pass over Melbourne with brief rain periods until 0500, followed by continuous stratiform rainfall until 1130 (continuous rainfall samples were obtained between 0630 and 1130), with substantial half-hourly accumulations.

[15] Radar reflectivities from the Australian Bureau of Meteorology M1500 S band volumetric radar illustrate a cellular structure within the stratiform rainbands, marking differences in spatial rainfall distribution and intensity. Of note are the 10–20 km scales of the convective elements and the gradients in rainfall intensity across the bay area. The radar image in Figure 3a captures the rainband toward the end of the MF-1 phase of the mixed frontal case study during which time the rainband was tracking across the bay area from the northwest to the southeast. A rain shadow from the surrounding hills can clearly be seen stretching between the northwestern townships of Gisborne and Melton, a distance of 21 km. A highly localized rainfall distribution is particularly evident in the summer convective case. The radar image from early in this event (Figure 3b) depicts the period of maximum rainfall intensity measured at the Melton site. A total of 20.5 mm was recorded at Melton during the half-hour period from which this scan was taken, which corresponds with the approximate rainfall intensity as measured by the radar for this location. Figure 3c illustrates the widespread rainfall during the stratiform case. The rainband tracked in a north-south direction and had a reduced shadow effect over the northern suburbs. Rainfall intensities were generally more intense than the MF-1 phase of the mixed frontal case, particularly over the southeastern bayside suburbs with rainfall rates greater than 20 mm h^{-1}.

3.3. Dynamically Constrained Isotope Simulations

[16] The dense, small-scale coverage of the MUNIP observations can be complemented by an expanded approach to the analyses of the case study events. Supplementing observational data with temperature and moisture fields derived from an isotopic GCM is one means of extension, provided the reliability of the model representation is known. In general, isotope GCMs may only be compared to observations in a statistical sense; however, by constraining the atmospheric circulation by periodic relaxation to reanalysis fields, it is possible to compare model output directly against observations. Here we apply the method of *Noone* [2006] where constrained atmospheric dynamics from the NCAR CAM3 model are used to force a complex isotope hydrology scheme based on the bulk transfer models of *Noone and Simmonds* [2002] and *Federer et al.* [1982] that use single-moment microphysics to calculate exchange processes between six categories of isotopic hydrometeor [*Noone and Sturm*, 2009]. Below-cloud reevaporative pro-

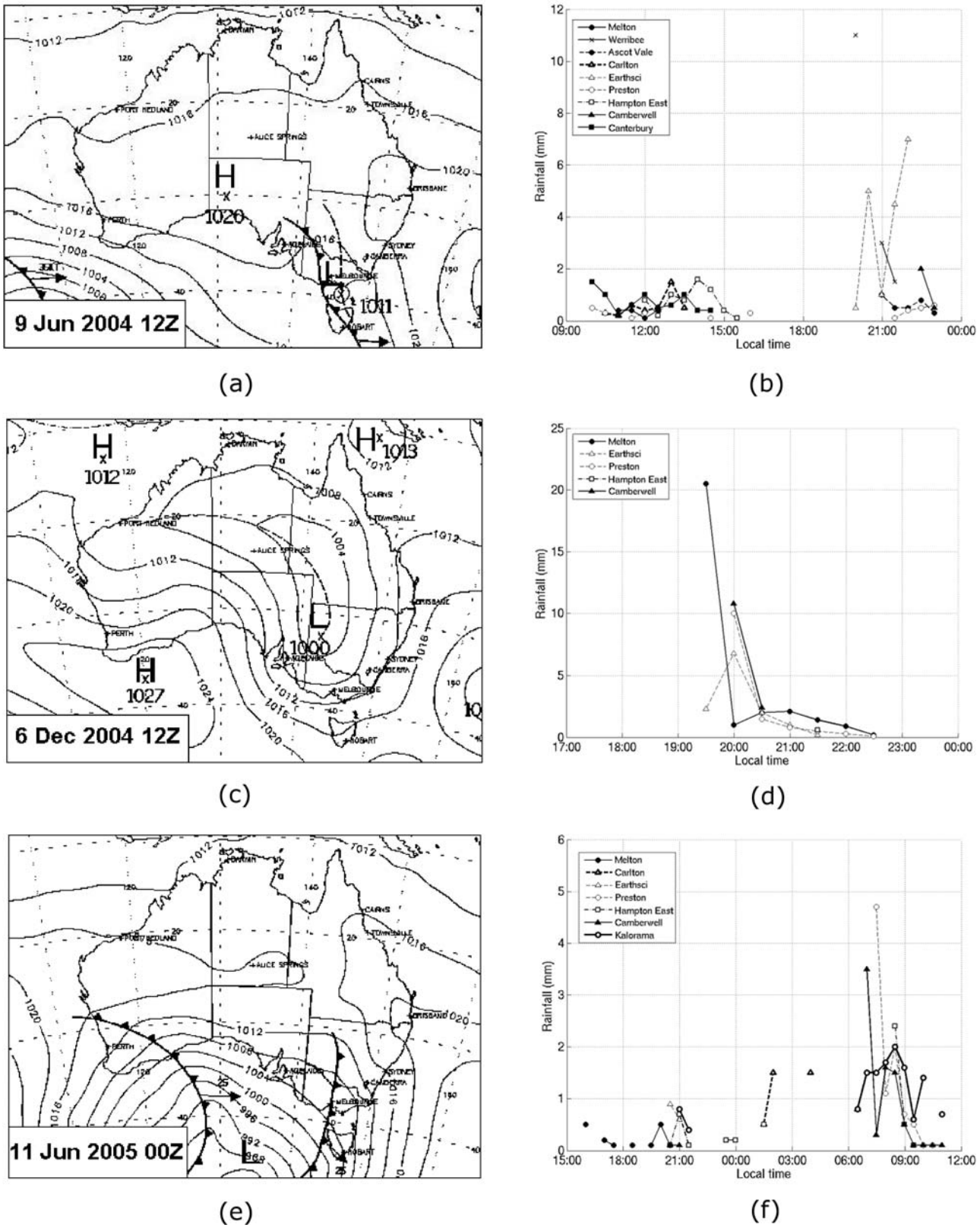

Figure 2. (left) Synoptic mean sea level pressure (MSLP) analyses and (right) MUNIP observed rainfall for (a and b) mixed frontal, (c and d) convective, and (e and f) stratiform case studies. Contour interval for MSLP is 4 hPa. Charts courtesy of the Australian Bureau of Meteorology. Note the different scales of the rainfall axes.

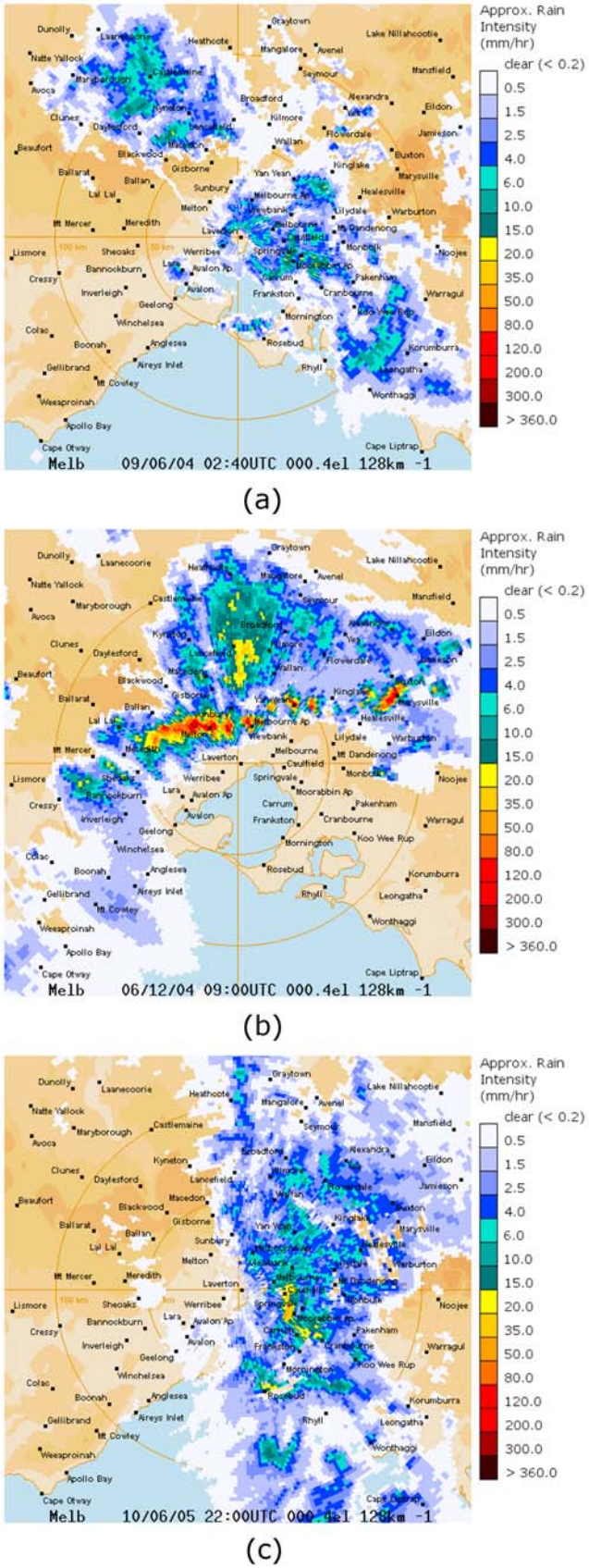

Figure 3. Volumetric radar images during key phases of (a) mixed frontal, (b) convective, and (c) stratiform rainfall events. Images courtesy Australian Bureau of Meteorology.

cesses are parameterized following *Stewart* [1975] and *Joussaume and Jouzel* [1993], who apply closed system total equilibrium fractionation to large-scale stratiform precipitation (small droplets with long residence times) and a Rayleigh distillation process with the inclusion of nonequilibrium kinetic effects for the larger droplets of convective precipitation. Beyond this, no further distinction is made between droplet sizes. The proportion of condensate permitted to equilibrate with the surrounding vapor is applied separately to the different types of precipitation identified by the model. In shallow convection and stratiform precipitation, this is 95%, whereas 100% equilibration is permitted in convective downdrafts, reducing to 35% for rain exiting the cloud base.

[17] For the running of the nudged simulations, global isotope fields are initialized from model climatology, and the boundary forcing conditions are adjusted during spin-up to match the reanalysis fields at the start of the simulation period. Fields of u, v, and T in the global model are used to dynamically constrain the GCM by relaxation toward data from the NCEP reanalysis [*Kalnay et al.*, 1996] at regular intervals, effectively limiting the model drift away from observations in these quantities. No nudging is performed on the isotope hydrology, leaving it to evolve freely driven by the constrained dynamics. Simulations are obtained via a sequence of short forecast runs. After initialization, a global forecast is made for 6 h. After this, the model forecast fields of u, v, and T at every grid point are relaxed toward the corresponding reanalysis fields such that

$$\hat{X} = X + \eta \frac{\Delta t}{\tau}(X_r - X), \tag{1}$$

where X and X_r are the model and corresponding reanalysis fields, respectively; Δt is the forecast period (6 h); τ is the relaxation time scale (24 h); and η is a scaling term that is set to unity at all levels above $\sigma = 0.850$ and decreases linearly from unity at $\sigma = 0.850$ to zero at $\sigma = 0.950$ in order that boundary layer conditions are determined predominantly by the parameterizations of the model. This process is repeated until the desired simulation period is obtained. Although momentum and energy are not conserved in this method, there is conservation of mass and vapor mass, which are important for accurate simulations of isotope fractionation [*Noone*, 2006]. Despite these physical approximations, the model hydrology in this configuration is capable of successfully simulating large-scale isotopic fields that are consistent with the synoptic circulation.

[18] For this investigation, global isotope simulations were run at a T42 (2.8° × 2.8°) resolution with 28 vertical levels for each of the MUNIP case studies for a number of days leading up to and including the event. It should be noted that by periodically forcing the model in this way, a small departure from the reanalyses is implicit in the model wind and temperature fields. Figures 4a, 4c, and 4e show the model mean sea level pressure of a representative period for each of the case studies overlaid with the corresponding NCEP reanalysis field. It can be seen that despite the departure mentioned above, the major circulation features and pressure gradients are represented well, with differences being mainly in subtle features and the depth of the systems (Figure 4b, 4d, and 4f). The model hydrology simulations

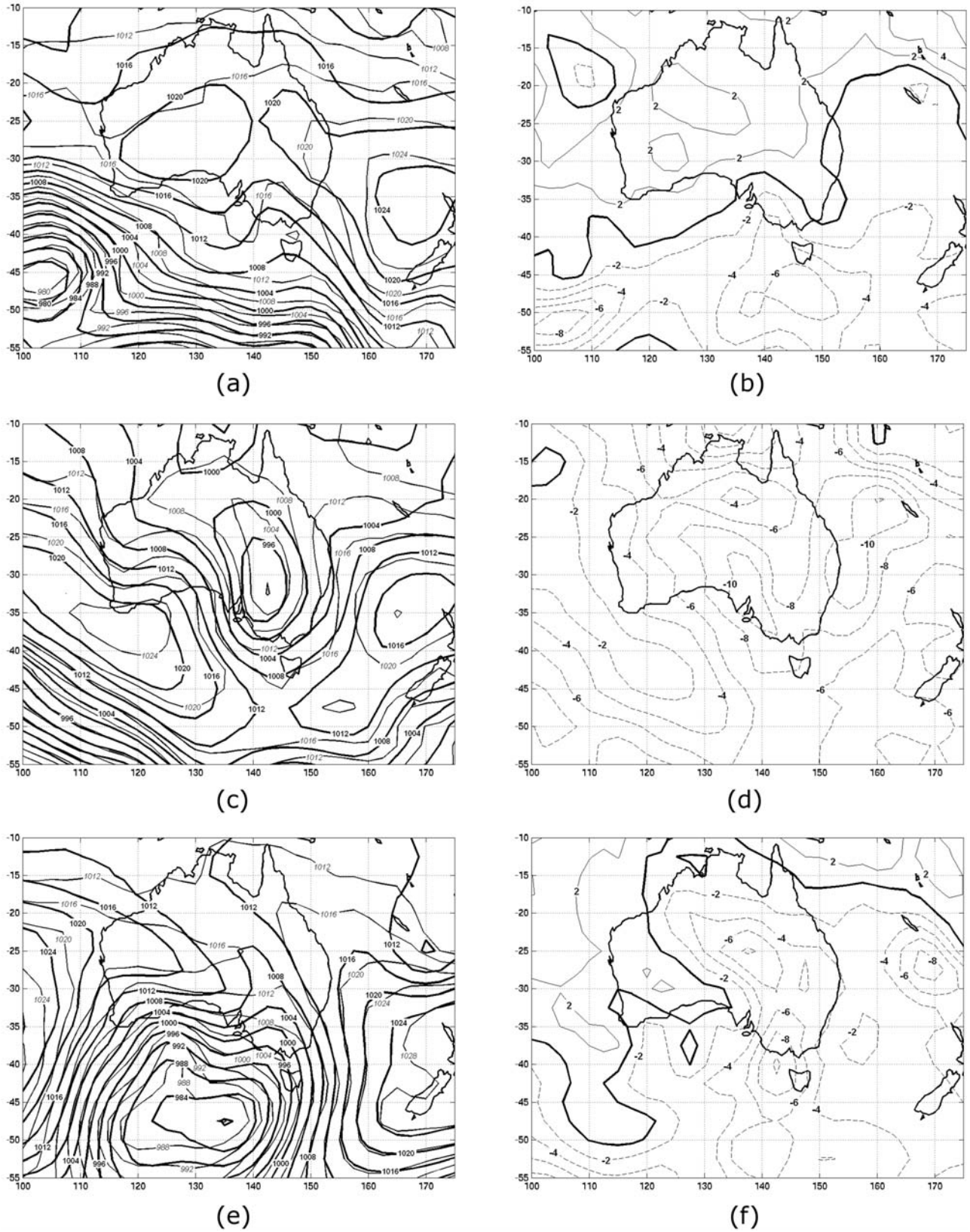

Figure 4. Comparison between CAM3 and NCEP2 synoptic MSLP for (a and b) mixed frontal, (c and d) convective, and (e and f) stratiform case studies. (left) Charts overlay maps for (bold numbers) CAM3 and (italic numbers) NCEP2. (right) Charts with corresponding difference field. Contour interval is 4 hPa for MSLP and 2 hPa for differences with zero contour in bold.

may be considered to be driven by a representative synoptic background. For more detailed analysis, data were taken from these global isotope simulations at a higher temporal resolution (20 min) in a column of 3 × 3 grid points centered over the nearest grid point to Melbourne, a land point slightly to the north and west of the actual location (37°S, 145°E), to examine the variability in isotope ratios over the study region driven by the large scale. The model was run for 12 h (commencement referred to as $t + 0$) after having been nudged toward the appropriate reanalysis field during assimilation. Data were then chosen from the $t + 6$ to $t + 12$ h period to minimize the effect of any physical imbalances that may have arisen during model spin-up. The six-hourly data were then concatenated to cover the desired MUNIP periods. Minor discontinuities in the data appeared at the intersection of each model run as a result of this process, which can be seen in Figures 7 and 8; however, as these are not significant in magnitude and the large-scale trends are continuous throughout the period, this was not deemed to be a problem.

4. Results

4.1. Observations of δ^{18}O and Deuterium Excess

[19] The observations of δ^{18}O and deuterium excess during the MUNIP IOPs show strong high-frequency variability between measurement intervals at each station. In addition, there are trends in the measurements that are common to all stations, a feature not able to be adequately resolved by single-point observations.

[20] Observed patterns of δ^{18}O for the mixed frontal case reflect the contrast in rainfall type between the subperiods MF-1 and MF-2 (Figure 5a). The most isotopically enriched rainfall was measured at the Preston site. This location received some of the lowest rainfall amounts during the stratiform MF-1 phase as it lay near the edge of a rain shadow from the northwestern mountains. A common trend of δ^{18}O depletion was measured at all sites during MF-1. Where data from more than one site were available, a mean rate of depletion of -0.3‰ h^{-1} was observed. Toward the end of the MF-1 period, δ^{18}O was enriched substantially at the Hampton East site as rainfall amounts decreased steadily. A similar pattern was observed at Carlton and Canterbury. The thunderstorms of the MF-2 phase occurred in short-lived and highly localized pulses of very intense rainfall as witnessed by observers. Despite this, the δ^{18}O variability remains largely uniform across the sampling sites during MF-2. In addition, a common background trend can again be seen in δ^{18}O with a mean depletion rate of -1.1‰ h^{-1}.

[21] Values of deuterium excess for the mixed frontal case were also highly variable between observation intervals, showing some sensitivity to rainfall amount (Figure 5b). The majority of values during MF-1 were below 10‰ with a median value of 6.5‰. During the MF-2 phase, the deuterium excess values became much greater, increasing in value significantly toward the end of the period.

[22] The temporal depletion of δ^{18}O during the convective case study did not follow the L-type pattern as is commonly observed in convective cases [*Celle-Jeanton et al.*, 2004] (Figure 5c). Melton was most severely affected by storm activity during this event, recording 20.5 mm in the first half hour and recording its most isotopically depleted rainfall. After this, a steady isotopic depletion was observed at this site at a more constant rainfall intensity for the next three collection intervals. At the remaining sites, after an initial pulse of convection during which the most depleted rainfall was measured, a gradual enrichment of δ^{18}O was observed under light rainfall conditions.

[23] The corresponding deuterium excess measurements (Figure 5d) followed the pattern of rainfall amount closely, beginning with large positive values followed by a steady decrease throughout the event. The common trend across all sites is an indicator of a uniformity of the moisture environment across the region.

[24] The stratiform case study was similar to the mixed frontal event in that it featured two separate rainfall events: scattered, light prefrontal rainfall (S-1) and continuous rainfall of moderate intensity (S-2). The sporadic precipitation of the S-1 phase prevents any detailed analysis of δ^{18}O; however, strong trends were observed during S-2 (Figure 5e). Values of δ^{18}O showed only a small variation during S-1, which continued until 0630 on 11 June, where a mean depletion rate of -3.6‰ h^{-1} was measured at the Preston, Camberwell, and Kalorama sites. This was followed by a steady enrichment in δ^{18}O as the rainfall intensity decreased. Corresponding deuterium excess values at these sites show rapid fluctuations throughout both phases of the event (Figure 5f). Values of deuterium excess remained below 10‰ during the S-1 phase; however, during S-2 the deuterium excess increased from zero to values greater than 4‰ as the rainfall became more widespread. As the rain intensity decreased toward the end of the event, the deuterium excess values decreased, while δ^{18}O showed a weak enrichment. The increase in δ^{18}O is characteristic of postfrontal rainfall following a minimum with the passage of the front [*Rindsberger et al.*, 1990]. The Kalorama site measured enrichment in δ^{18}O; however, deuterium excess also increased at this location at 1000 as a local pulse of rainfall from an embedded convective cell passed over the site. Here the deuterium excess indicated a local change not clearly resolved by δ^{18}O.

[25] The general pattern of δ^{18}O variability during the three case studies was a steady shift in the relative importance of microphysical and large-scale effects. The pattern for stratiform precipitation featured high-frequency variation overlaid upon a background steady depletion. Under convective conditions, values of deuterium excess showed a positive association with rainfall amount (Figure 6). On such short measurement time scales, deuterium excess was sensitive to short periods of rapidly changing rainfall intensities. Despite the cellular structure of the stratiform rainbands as indicated by the radar imagery, periods of stratiform rainfall featured a less defined variation of deuterium excess with rainfall amount indicating the presence of additional influences on falling droplets. The patterns observed are consistent with the understanding that under the less intense stratiform rainfall conditions, there is a greater proportion of droplet equilibration with the background environmental vapor due to a smaller droplet size distribution [*Laws and Parsons*, 1943; *Marshall and Palmer*, 1948; *Feingold and Levin*, 1986; *Ignaccolo et al.*,

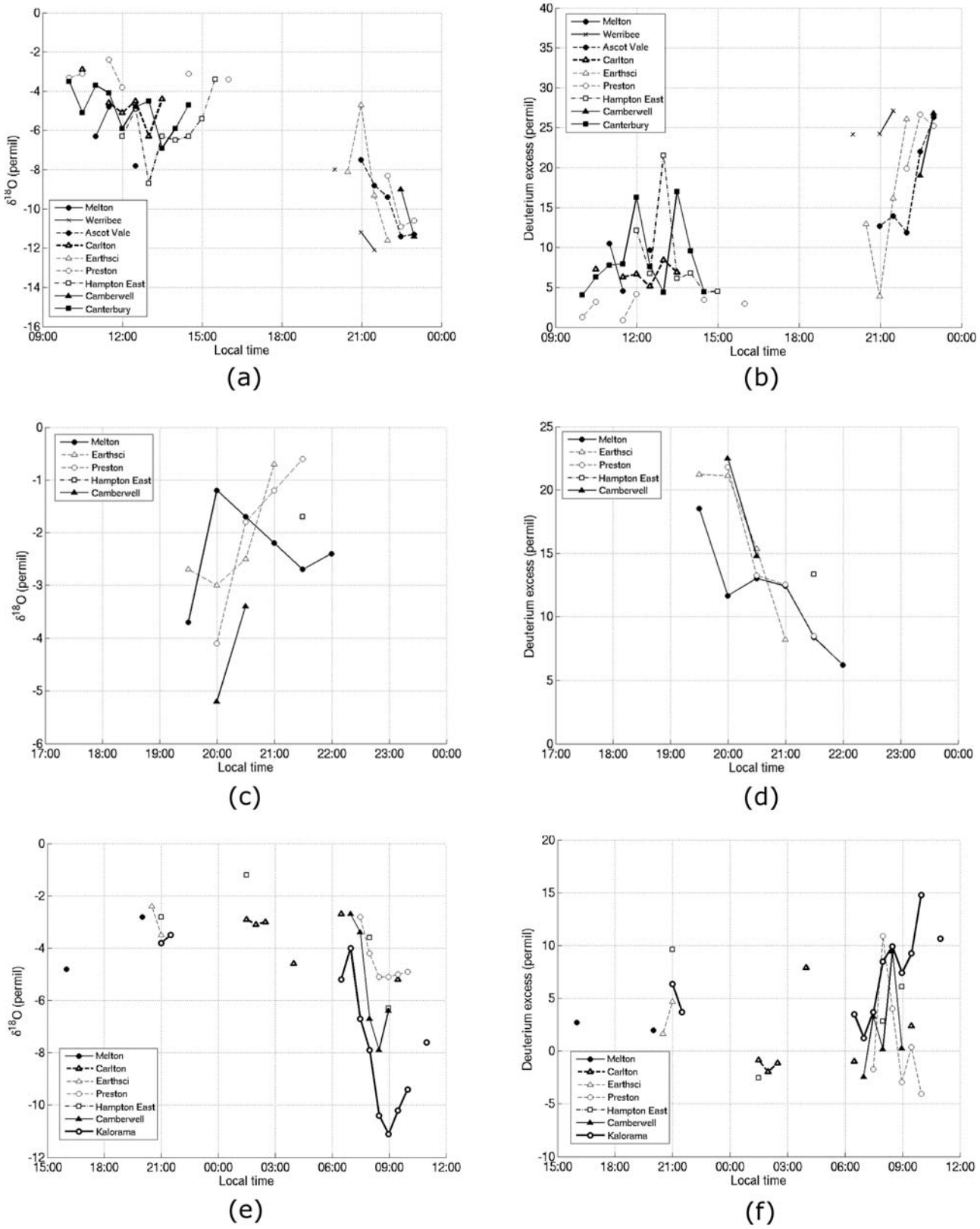

Figure 5. MUNIP half-hourly observations of (left) $\delta^{18}O$ and (right) deuterium excess for (a and b) mixed frontal, (c and d) convective, and (e and f) stratiform case studies.

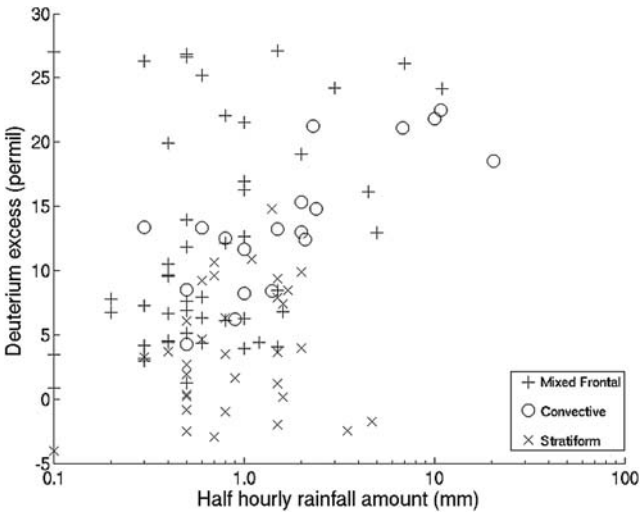

Figure 6. Observed deuterium excess with log transform half-hourly rainfall amount for the MUNIP case studies.

2009] and a reduction in droplet equilibration time [*Stewart*, 1975; *Jouzel*, 1986].

[26] A complicating factor associated with the observations themselves is that by sampling rainfall amounts at half-hourly intervals, observations of rain amount may only be considered representative of rainfall intensity if this were constant across the collection period. As indicated by the radar imagery in Figure 3, rainfall intensity tended to vary on much smaller time scales because of the embedded cellular structure of stratiform rainbands. Therefore, in some cases of small rainfall amounts with high deuterium excess, these accumulated during short but intense rainfall periods.

4.2. CAM3 Isotope Simulations

[27] Observations of $\delta^{18}O$ variability during each case study reflected a change in the relative importance of small- and large-scale isotope effects. Isotope effects governed by the large scale may be quantified by noting the structure and changes in the profiles of low tropospheric water vapor over time and by examining the moisture history of the air masses. Data coverage on such scales is made possible by supplementing the observations with isotope model simulations, provided the model is sufficiently accurate. Because the influence of the large scale was of interest, the dynamically constrained NCAR CAM3 GCM (described in section 3.3) was suitable for this purpose. The coarseness of the model resolution precluded it from providing detailed information in the convective case; therefore, the CAM3 simulations were confined to the mixed frontal and stratiform events.

4.2.1. Mixed Frontal Case

[28] Model fields of $\delta^{18}O$ and deuterium excess in precipitation and water vapor and the temperature for the mixed frontal case study are presented in Figure 7. Overall, the model represents the magnitude of depletion with some accuracy, although it sustains stratiform precipitation throughout the period. Inferences drawn from the model may at least be applied with some confidence for the MF-1 phase of precipitation. Model rainfall accumulation remains steady at 1.2 mm h^{-1} with a corresponding rate of depletion of -0.5‰ h^{-1} (Figure 7a). The simulated deuterium excess similarly decreases steadily, but average values are much greater than those observed. The temperature of the column remains relatively constant with time at all levels in the low troposphere and steadily decreases with height (Figure 7b). With such a temperature profile, it would be expected that the vertical profile of $\delta^{18}O$ in vapor ($\delta^{18}O_v$) would similarly decrease steadily with height. However, two regions of very weak vertical gradient are present at the levels around 750 and 950 hPa in the initial $\delta^{18}O_v$ profile characterized by ratios of -22‰ and -16‰, respectively (Figure 7c). This initial profile structure may reflect different moisture histories of air masses at these levels and is investigated further using trajectory reconstructions in section 4.2.3. As the event progresses, a weak depletion of $\delta^{18}O_v$ can be seen throughout the column below 700 hPa. Assuming Rayleigh condensation at 10°C, the $\delta^{18}O$ of model precipitation ($\delta^{18}O_p$) at the beginning of the simulation (-4.5‰) corresponds with moisture equilibrating with vapor near the surface (-15.2‰ at 980 hPa). As an illustration of the extent of vapor depletion during the event, an estimate of rainout was found by analyzing the depletion of the saturated layer (between 750 and 650 hPa in observed soundings). At this level, vapor depletion was around 2‰ immediately prior to the model run overlap at 1700. To allow for the fact that precipitation was being formed from ascending air rather than falling solely from 700 hPa, the condensation temperature was set to be the mean column temperature (6°C). The vapor depletion of the profile equates to a rainout of 11% of the moisture from the start of the period. Depletion of the vapor continues under stratiform conditions beyond the overlap by a further 3‰ until the end of the simulation. Combined, this represents 22% rainout across the entire period. The corresponding time section of deuterium excess in vapor shows a weak change over time and a positive vertical gradient (Figure 7d). This may be an indication of different moisture origins for the air masses at different levels, with the upper level moisture featuring a slightly greater deuterium excess. Early on, there is a brief drawing aloft of the low-level moisture into this upper air mass. The low-level deuterium excess decreases weakly throughout the simulation, which may be an indication of mixing with the moisture falling from aloft.

4.2.2. Stratiform Case

[29] The sharp depletion in $\delta^{18}O_p$ observed during the stratiform event is represented by CAM3; however, the onset of precipitation in the model is early by around 12 hours (Figure 8a). This does not necessarily make the simulation incorrect, as rainfall was indeed observed over southern Victoria at this time. However, the entire Port Phillip Bay area was under a rain shadow cast by the low mountain range to the northwest, a feature unable to be resolved by CAM3. Despite this, the model is still useful in the representation of the large-scale effects of the event.

[30] The model depicts a steady depletion of the $\delta^{18}O_p$ ratios from the beginning of the event until 0700 the following day. The maximum rate of depletion in the simulation is -2.2‰ h^{-1} between 1800 and 2200, less than the observed rate of -3.6‰ h^{-1}. A decrease is also seen early in the model deuterium excess values, but these stabilize around a value of 17‰ soon after, much higher than observed, as seen in the mixed frontal simulation. The

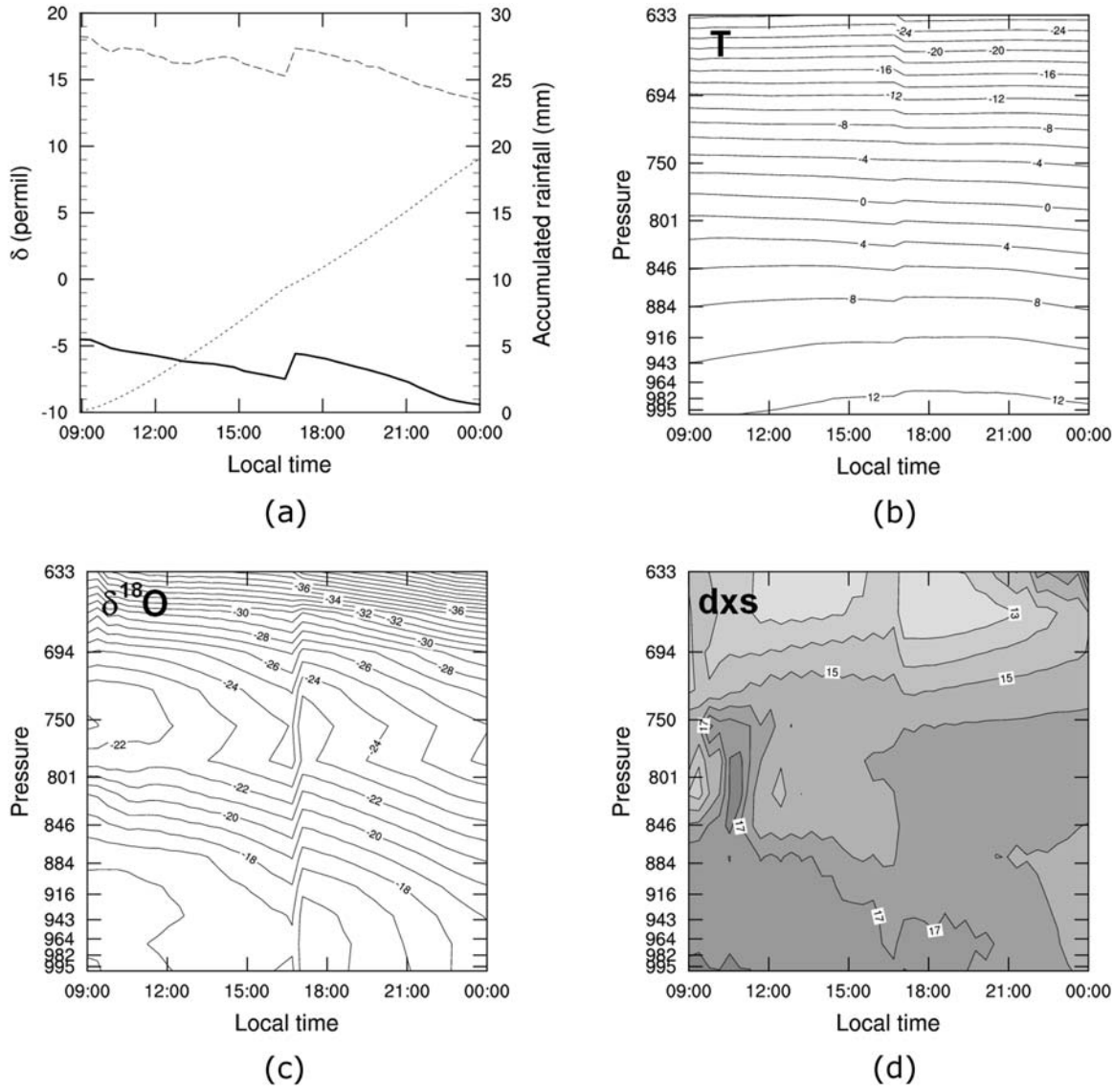

Figure 7. CAM3 isotope simulation at Melbourne grid point for MUNIP mixed frontal case study (a) time series of $\delta^{18}O$ (solid line) and deuterium excess (dashed line) in precipitation and accumulated rainfall (dotted line), (b) temperature (°C), (c) $\delta^{18}O_v$ (‰), and (d) deuterium excess (‰).

temperature profile of the column remains largely unchanged throughout the simulation as with the previous case (Figure 8b); however, temperature changes due to the passage of the front were unable to be resolved by the model assimilation of 6-hourly reanalyses. Unlike the mixed frontal case, the initial vertical profile of $\delta^{18}O_v$ shows a steady depletion with height, much more in accordance with the temperature profile. As the simulation progresses, a strong depletion can be seen in $\delta^{18}O_v$, particularly in the model levels below 800 hPa (Figure 8c). Following the same assumptions of section 4.2.1, an estimate of rainout was made by noting 12‰ vapor depletion at 950 hPa prior to the model overlap assuming a condensation temperature of 12°C. This led to an estimate of 61% rainout from the beginning of the simulation at a depletion rate of 1.2‰ h^{-1}. There is a further depletion of $\delta^{18}O_v$ beyond the overlap until 0300, when the isotopic content of the vapor stabilizes in the layers below 850 hPa. Above this level, there is a gradual enrichment of the vapor from advection of less depleted moisture from the west. With rainfall still continuing at the same rate a balance appears to be established between the rate of depletion from condensation and the replenishment rate from advection below 850 hPa. There is little variation in the distribution of deuterium excess (Figure 8d), with precipitation values largely determined by near surface fluctuations.

4.2.3. Three-Dimensional Backward Trajectories

[31] The initial $\delta^{18}O_v$ profile for the mixed frontal case study identified two regions of particularly weak isotopic gradient (see Figure 7c). It is of interest here to examine the moisture history of this event and determine the trajectories of moist air masses arriving at different levels over Melbourne. This was done using a 3-D Lagrangian trajectory scheme (described in Appendix A) calculating the five 6-day backward trajectories for air masses arriving at 0000 UT (1000 LT) in Melbourne at the 950, 900, 850,

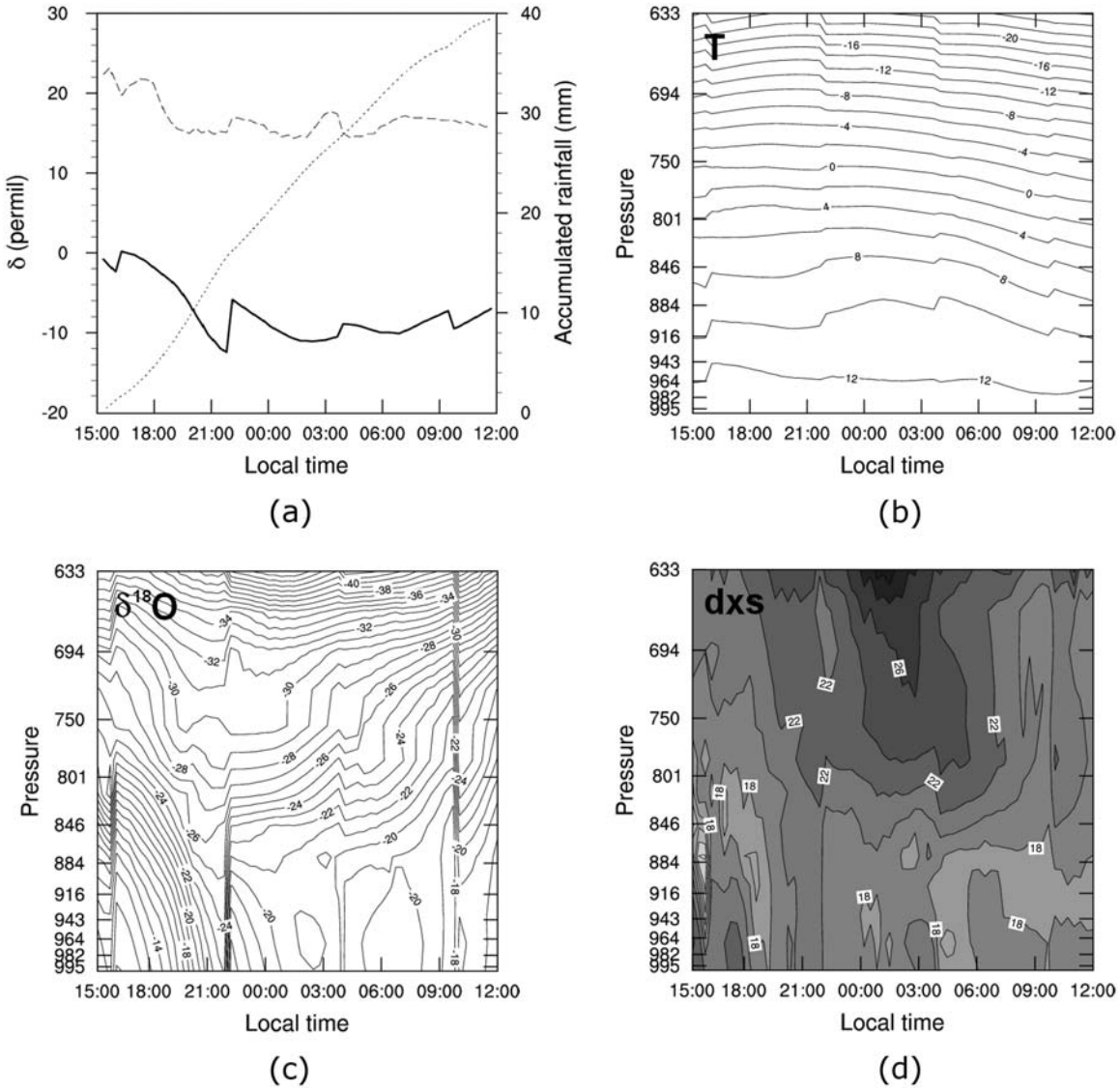

Figure 8. CAM3 isotope simulation at Melbourne grid point for stratiform case study (a) time series of δ^{18}O (solid line) and deuterium excess (dashed line) in precipitation and accumulated rainfall (dotted line), (b) temperature (°C), (c) $\delta^{18}O_v$ (‰), and (d) deuterium excess (‰).

700, and 500 hPa levels. The trajectory paths reveal a substantial difference in moisture origin between the air masses arriving at the lowest two levels (Figure 9a) and those above. Trajectories 1 (arriving at 950 hPa) and 2 (900 hPa) were sourced off the east coast of Australia and looped inland over the continent before arrival. Air masses arriving at higher levels also passed across the continent but were sourced from the northwest. Therefore, the isotope ratios of precipitation collected at the surface were a mixture of moisture from two different moisture sources. This is consistent with the structure of the model moisture profiles for this event.

[32] Using the global isotope fields of $\delta^{18}O_v$, deuterium excess, and temperature from the CAM3 simulations, moisture histories were constructed for the 64 h period prior to arrival (denoted $t - 0$ h) for air masses arriving at the five levels mentioned above. Changes in temperature (Figure 9b) closely followed changes in altitude, with trajectories 1 and 2 gradually descending and warming until $t - 24$, then weakly cooling with ascent from $t - 12$. A similar trend is seen with trajectory 3. Trajectory 4 (arriving at 700 hPa) remained at a near-constant temperature as it passed across the southern coastline of Australia, then began cooling with ascent around $t - 18$. Cooling was particularly strong with trajectory 5 (500 hPa) under continuous ascent. Little change was seen in either the $\delta^{18}O_v$ or deuterium excess of trajectories 1–4 during the approach period until $t - 18$. The $\delta^{18}O_v$ of the low air masses (trajectories 1–3) were only slightly modified (Figure 9c), whereas a stronger depletion was seen with trajectory 4. For each trajectory, precipitation was negligible prior to the mixed frontal event until $t - 24$ for trajectories 4 and 5, where light precipitation fell at these locations (from the atmospheric column, not necessarily from those levels). Fluctuations were greatest for trajectory 5. However, there is little moisture in the midtroposphere, and there is a sharp moisture gradient

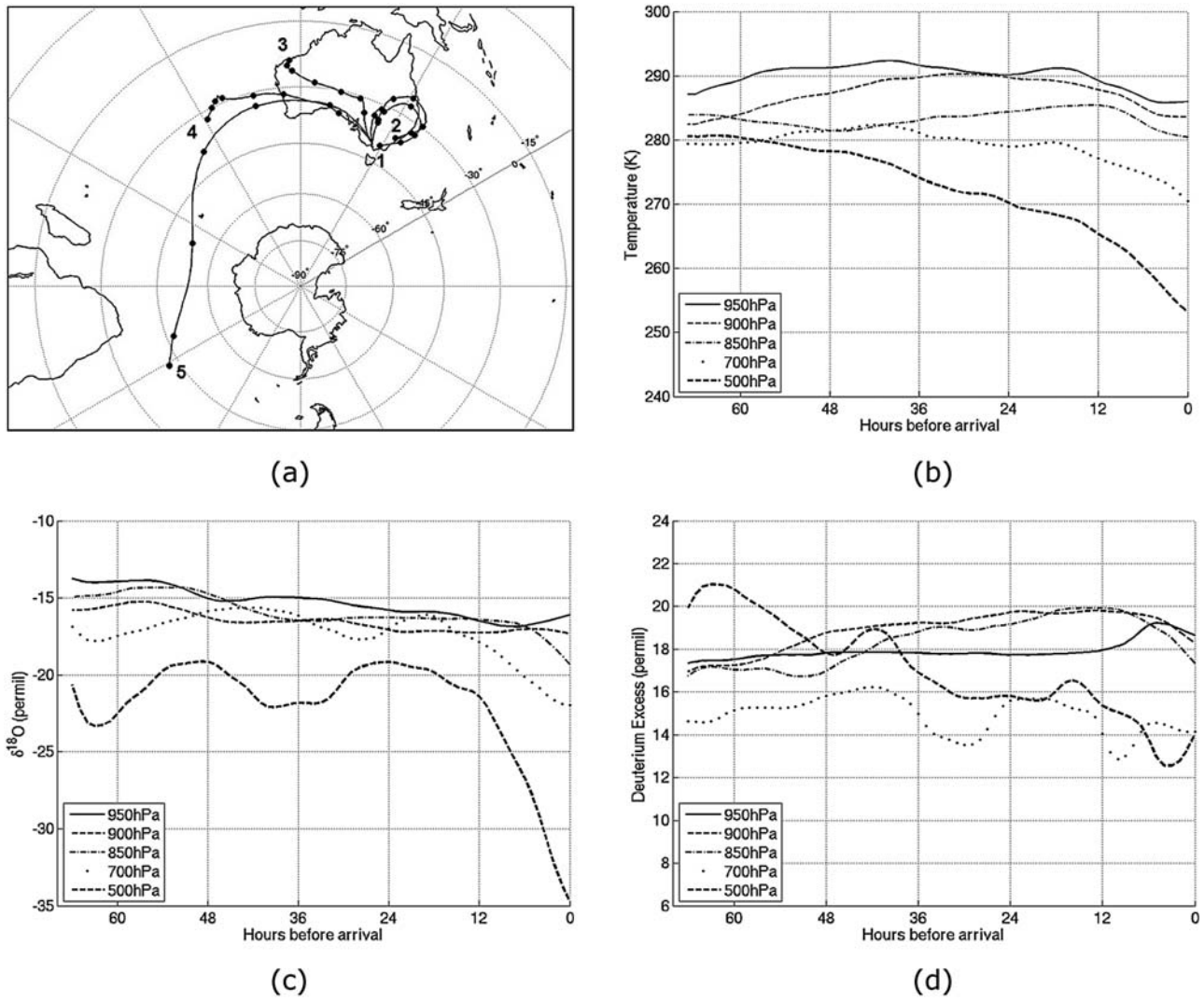

Figure 9. Three-dimensional backward trajectories arriving in Melbourne calculated for mixed frontal case study. (a) Back trajectories (144 h) calculated from NCEP wind fields. Trajectories labeled 1–5 are those arriving at 950, 900, 850, 700, and 500 hPa, respectively. Dots mark 24 h intervals. CAM3 isotope trajectories (72 h) arriving at the same levels for (b) temperature, (c) $\delta^{18}O_v$, and (d) deuterium excess (vapor).

immediately below; therefore, values would be highly sensitive to the influx of moisture from lower levels. As with $\delta^{18}O_v$, the deuterium excess of the vapor remained steady during approach (Figure 9d) as condensation and mixing occur in the model at equilibrium. It is of note that there is a substantial difference in the values of deuterium excess between the low-level trajectories (1–3) and those higher up (4–5) upon arrival at $t - 0$. This difference is reflected in the initial profile of deuterium excess in Figure 7d.

5. Discussion

[33] A unified approach of observation and modeling has provided a number of useful insights into the atmospheric conditions affecting the isotope ratios of precipitation of the MUNIP IOPs. The measurements of $\delta^{18}O$ by the MUNIP network resembled patterns of frontal precipitation observed in the Northern Hemisphere [*Miyake et al.*, 1968; *Rindsberger et al.*, 1990; *Pionke and DeWalle*, 1992; *Celle-Jeanton et al.*, 2004]. On these intraevent time scales, there are common large-scale trends in $\delta^{18}O$ overlaid by high-frequency variability at each station. This pattern may be seen as a continual change in the relative importance of the effects of changing rain intensity from mesoscale convection and rainout from large-scale precipitation. During the passage of stratiform rainbands, the MUNIP observations indicated that brief increases in rainfall intensity arising from embedded convective cells often yielded more depleted rainfall. This was more apparent under the strong convective conditions of the summer convective event that featured longer periods of intense precipitation. Increases in rainfall intensity relate to increases in droplet size, as discussed by *Feingold and Levin* [1986] and *Ignaccolo et al.* [2009], which has a direct bearing upon droplet fall speed and equilibration

Table 1. Regression Equations for the Melbourne International Atomic Energy Agency Data, 1962–1998, and Melbourne University Network of Isotopes in Precipitation Observed and Modeled Case Studies

	Observed Regression			CAM3 Regression		
Case Study	Equation	n	r^2	Equation	n	r^2
Melbourne IAEA	$\delta^2H = 7.1\ \delta^{18}O + 7.0$	324	0.93	...	...	...
Mixed frontal	$\delta^2H = 5.3\ \delta^{18}O - 6.2$	50	0.95	$\delta^2H = 9.3\ \delta^{18}O + 20.8$	90	0.99
Convective	$\delta^2H = 4.6\ \delta^{18}O + 6.4$	17	0.75	$\delta^2H = 6.0\ \delta^{18}O + 4.7$	55	0.71
Stratiform	$\delta^2H = 6.8\ \delta^{18}O - 2.6$	36	0.95	$\delta^2H = 8.4\ \delta^{18}O + 19.4$	108	0.99

time with the background environmental vapor [*Bolin*, 1958; *Stewart*, 1975; *Jouzel*, 1986; *Lee and Fung*, 2008, *Noone and Sturm*, 2009]. Under convective conditions with intense rainfall, a positive relationship was found between rainfall amount (approximating intensity) and deuterium excess. As depicted by radar imagery, the cellular structure of stratiform precipitation indicates that a similar relationship is also likely to exist under these conditions. However, this relationship is weak when compared to the effect of droplet equilibration with the surrounding environmental vapor, behavior consistent with generally smaller droplet sizes under stratiform conditions.

[34] Simulations of these events using a dynamically constrained isotope GCM enabled further exploration of the large-scale conditions contributing to the observed isotope variability. Despite some shortcomings in the representation of particular details of the mixed frontal and stratiform events, the model simulation did capture important features seen in the observations. Of greatest value was the simulation of the time evolution of vertical profiles of $\delta^{18}O_v$. The model $\delta^{18}O_v$ profiles for the MF-1 phase of the mixed frontal case revealed two regions of particularly weak vertical gradient, whereas the profiles for the stratiform event corresponded more closely with the model temperature profile. Trajectory analysis has been particularly informative for the mixed frontal event by showing that the structure of the model vapor profiles of $\delta^{18}O_v$ and deuterium excess were a reflection of the convergence of differently sourced air masses over Melbourne at different levels. In understanding the isotopic ratios in precipitation for the mixed frontal event, it should be considered that moisture falling from aloft was equilibrating with near-surface vapor drawn from a completely different moisture source. The model represented well the observed sharp decrease in $\delta^{18}O_p$ observed during the stratiform event despite mistiming the onset of precipitation. The strong depletion in $\delta^{18}O_v$ in the low troposphere illustrated the substantial effect of rainout on the low-level moisture profile. Vapor advection in the model was also shown by substantial changes in the $\delta^{18}O_v$ profile during the latter stages of the stratiform event simulation, having an enriching effect on modeled precipitation.

[35] Less conclusive were the changes in the simulated precipitation values of deuterium excess. The simulations showed that, despite the parameterization of kinetic isotope enrichment of droplets below the cloud base in the model, the values of deuterium excess were considerably greater than those observed. This may be due to an underestimation of the change in the δ^2H–$\delta^{18}O$ relationship brought about by the parameterization of kinetic isotope fractionation by an "effective fractionation coefficient" [*Jouzel et al.*, 1987; *Joussaume and Jouzel*, 1993]. Under the nonequilibrium conditions of kinetic isotope fractionation, the small difference in molecular diffusivity of ^2H and ^{18}O tends to reduce the slope of the δ^2H–$\delta^{18}O$ relationship [*Joussaume and Jouzel*, 1993]. The rate of molecular exchange is sensitive to changes in the relative humidity and $\delta^{18}O_v$ of the atmosphere and the temperature-dependent fractionation factors [*Gat*, 1996]. Comparisons of the observed and simulated δ^2H–$\delta^{18}O$ regression equations for precipitation show the model systematically overestimated the δ^2H–$\delta^{18}O$ slope (Table 1), which would lead to model overestimations of deuterium excess. Some local tuning of the extent of condensate equilibration may be required to bring these values more into agreement with the observations. One possibility is a reduction in the percentage equilibration applied to stratiform rainfall to increase the extent of kinetic effect adjustment. More sophisticated isotope models such as that of *Lee et al.* [2007] have begun to incorporate parameterizations of droplet size distribution into calculations of postcondensation exchange to better represent changes in the extent of equilibration that differ not only with rainfall type but also across the regions of the world [*Lee and Fung*, 2008].

6. Conclusion

[36] The variation in the ratios of ^{18}O and deuterium excess were investigated by high-frequency sampling of rainwater from three weather systems passing across Melbourne, Australia. By combining observations with simulations from a dynamically constrained GCM, the general patterns of isotopic variability on intraevent time scales were found to be consistent with large-scale trends in $\delta^{18}O$ driven by Rayleigh-type rainout overlaid by high-frequency variability associated with changes in rainfall amount. Deuterium excess fluctuated with rainfall amount due to its sensitivity to nonequilibrium fractionation occurring during the fall of droplets. Under convective conditions, high values of deuterium excess were associated with periods of higher rainfall intensity; however, this relationship was less well defined during stratiform precipitation.

[37] Modeling the events with a version of NCAR CAM3 by periodic nudging of dynamic fields to reanalyses provided a valuable insight into the isotopic evolution of $\delta^{18}O$ and deuterium excess during the events. Despite a relatively coarse resolution, the model represented well the major features of isotopic variability under stratiform conditions. The extended data coverage supplied by the model data provided detail of the evolution of vertical vapor profiles

and enabled estimates of the extent of rainout during observed events. Trajectories run for the mixed frontal case reconstructed the likely moisture history of the event, indicating that the initial profile of $\delta^{18}O_v$ arose from a convergence of air masses with completely different moisture origins. The model did overestimate the δ^2H–$\delta^{18}O$ relationship for precipitation, resulting in overestimations of the deuterium excess; however, this may be addressed with adjustment of the postcondensation parameterizations to local conditions.

[38] Isotopic modeling here has been useful in supplementing the data coverage of typical rain events affecting southeastern Australia, providing valuable detail of the structure and history of the events that would not be available from the sampling of precipitation alone. With the advent of more sophisticated models incorporating more detailed isotopic fractionation schemes, there is a need for more high-resolution observational studies, particularly targeting subcloud postcondensation processes and vapor advection. Future investigations would benefit from the increased temporal resolution provided by ongoing in situ sampling of vapor using portable infrared diode laser spectrometers [*Webster and Heymsfield*, 2003] in conjunction with satellite-derived water vapor isotope profiles [*Worden et al.*, 2006; *Helliker and Noone*, 2009]. Targeted observation and modeling in this way will provide a useful framework for the ongoing development of isotopic models.

Appendix A: Three-Dimensional Spherical Trajectory Algorithm

[39] The 3-D trajectory scheme used in this study is that described by *Noone and Simmonds* [1999], which itself was an enhancement of the 2-D formulation of *Law* [1993] that was also used by *Perrin and Simmonds* [1995]. Using 3-D wind fields, the scheme solves the prognostic equation for the trajectory path:

$$\bar{x}_{n+1} = \bar{x}_n + \overline{V}\Delta t, \tag{A1}$$

where Δt is a suitably short time interval and the wind field at the trajectory parcel location ($\overline{V}$) is found by bicubic interpolation. For the calculation of backward trajectories, the direction of the winds is reversed and interpolated linearly in time. The prognostic equation (A1) is solved using a fourth-order Runge-Kutta method such that $\overline{V} = (1/6)(\overline{V}_1 + 2\overline{V}_2 + 2\overline{V}_3 + \overline{V}_4)$ in order to obtain a sufficiently accurate trajectory path between time steps. The scheme uses spherical coordinates in the horizontal and sigma levels in the vertical. Parcel locations are determined according to

$$\theta_{n+1} = \sin^{-1}\left(\cos(D)\sin(\theta_n) + \sin(D)\cos(\theta_n)\cos(\phi)\right), \tag{A2}$$

$$\lambda_{n+1} = \lambda_n + \left(\frac{u}{|u|}\right)\sin^{-1}\left(\frac{\sin(D)\sin(\phi)}{\cos(\theta_{n+1})}\right), \tag{A3}$$

$$\sigma_{n+1} = \sigma_n + \dot{\sigma}\Delta t, \tag{A4}$$

where the radian distance of trajectory motion (D) is given by

$$D = \frac{\Delta t\sqrt{u^2 + v^2}}{R}, \qquad R = 6.37 \times 10^6 \text{ m} \tag{A5}$$

and the direction of motion is given by

$$\phi = \frac{\pi}{2} - \tan^{-1}\left(\frac{v}{u}\right). \tag{A6}$$

Using the same formulation, the scheme is also capable of following the evolving characteristics of an air parcel along its trajectory driven by the large scale. There is presently no additional modification included for the effects of small-scale processes (e.g., latent heating due to condensation and sub-grid-scale motions).

[40] **Acknowledgments.** We are indebted to the efforts of the MUNIP observation team in the accumulation of the observations. Thanks go to David Etheridge, Christen Barras, Lynette Bettio, Pandora Hope, Kevin Keay, Eunpa Lim, Chris Pickett-Heaps, and Richard Wardle. NCAR CAM3 data and much useful advice were kindly provided by David Noone at the University of Colorado. Our thanks also go to Tamie Weaver, Ian Cartwright, and Ben Petrides at Monash University for advice on collection methods and for performing the isotope analyses. This work was supported by funding from the Australian Research Council, a Commonwealth Postgraduate Studentship from CSIRO Marine and Atmospheric Research, and a research scholarship from the University of Melbourne. The authors would also like to thank three anonymous reviewers for their comments, which greatly improved the manuscript.

References

Angert, A., J. Lee, and D. Yakir (2008), Seasonal variations in the isotopic composition of near-surface water vapor in the eastern Mediterranean, *Tellus, Ser. B*, *60*, 674–684.

Argiriou, A. A., and S. Lykoudis (2006), Isotopic composition of precipitation in Greece, *J. Hydrol.*, *327*, 486–495, doi:10.1016/j.jhydrol.2005.11.053.

Barras, V. J. I., and I. Simmonds (2008), Synoptic controls upon $\delta^{18}O$ in southern Tasmanian precipitation, *Geophys. Res. Lett.*, *35*, L02707, doi:10.1029/2007GL031835.

Bolin, B. (1958), On the uses of tritium as a tracer for water in nature, in *Proceedings of the 2nd UN Conference on the Peaceful Uses of Atomic Energy*, vol. 18, 336–343, Int. At. Energy Agency, Vienna.

Bony, S., C. Risi, and F. Vimeux (2008), Influence of convective processes on the isotopic composition ($\delta^{18}O$ and δD) of precipitation and water vapor in the tropics: 1. Radiative-convective equilibrium and Tropical Ocean–Global Atmosphere–Coupled Ocean-Atmosphere Response (TOGA-COARE) simulations, *J. Geophys. Res.*, *113*, D19305, doi:10.1029/2008JD009942.

Burnett, A. W., H. T. Mullins, and W. T. Patterson (2004), Relationship between atmospheric circulation and winter precipitation $\delta^{18}O$ in central New York State, *Geophys. Res. Lett.*, *31*, L22209, doi:10.1029/2004GL021089.

Celle-Jeanton, H., Y. Travi, and B. Blavoux (2001), Isotopic typology of the precipitation in the western Mediterranean region at three different time scales, *Geophys. Res. Lett.*, *28*, 1215–1218, doi:10.1029/2000GL012407.

Celle-Jeanton, H., R. Gonfiantini, Y. Travi, and B. Sol (2004), Oxygen-18 variations of rainwater during precipitation: Application of the Rayleigh model to selected rainfalls in southern France, *J. Hydrol.*, *289*, 165–177, doi:10.1016/j.jhydrol.2003.11.017.

Collins, W. D., P. J. Rasch, B. A. Boville, J. J. Hack, J. R. McCaa, D. L. Williamson, B. P. Briegleb, C. M. Bitz, S.-J. Lin, and M. Zhang (2006), The formulation and atmospheric simulation of the Community Atmosphere Model, version 3 (CAM3), *J. Clim.*, *19*, 2144–2161, doi:10.1175/JCLI3760.1.

Coplen, T. B. (1988), Normalization of oxygen and hydrogen isotope data, *Chem. Geol.*, *72*, 293–297.

Craig, H., and L. Gordon (1965), Deuterium and oxygen 18 variations in the ocean and marine atmosphere, in *Stable Isotopes in Oceanographic Studies and Paleotemperatures, Spoleto 1965*, edited by E. Tongiorgi, pp. 9–130, Cons. Naz. della Ric., Pisa, Italy.

Dansgaard, W. (1953), The abundance of ^{18}O in atmospheric water and water vapor, *Tellus*, *5*, 461–469.

Dansgaard, W. (1964), Stable isotopes in precipitation, *Tellus*, *16*, 436–468.

Fandry, C. B., and L. M. Leslie (1984), A two-layer quasi-geostrophic model of summer trough formation in the Australian subtropical easterlies, *J. Atmos. Sci.*, *41*, 807–818, doi:10.1175/1520-0469(1984)041<0807:ATLQGM>2.0.CO;2.

Federer, B., N. Brichet, and J. Jouzel (1982), Stable isotopes in hailstones. Part 1: The isotopic cloud model, *J. Atmos. Sci.*, *39*, 1323–1335, doi:10.1175/1520-0469(1982)039<1323:SIIHPI>2.0.CO;2.

Feingold, G., and Z. Levin (1986), The lognormal distribution fir to raindrop spectra from convective clouds in Israel, *J. Clim. Appl. Meteorol.*, *25*, 1346–1363, doi:10.1175/1520-0450(1986)025<1346:TLFTRS>2.0.CO;2.

Friedman, I., J. M. Harris, G. I. Smith, and C. A. Johnson (2002a), Stable isotope compositions of waters in the Great Basin, United States: 1. Airmass trajectories, *J. Geophys. Res.*, *107*(D19), 4400, doi:10.1029/2001JD000565.

Friedman, I., G. I. Smith, C. A. Johnson, and R. J. Moscati (2002b), Stable isotope compositions of waters in the Great Basin, United States: 2. Modern precipitation, *J. Geophys. Res.*, *107*(D19), 4401, doi:10.1029/2001JD000566.

Gat, J. R. (1996), Oxygen and hydrogen isotopes in the hydrologic cycle, *Annu. Rev. Earth Planet. Sci.*, *24*, 225–262, doi:10.1146/annurev.earth.24.1.225.

Gedzelman, S. D., and J. R. Lawrence (1982), The isotopic composition of cyclonic precipitation, *J. Appl. Meteorol.*, *21*, 1385–1404, doi:10.1175/1520-0450(1982)021<1385:TICOCP>2.0.CO;2.

Gonfiantini, R. (1986), Environmental isotopes in lake studies, in *Handbook of Environmental Isotope Geochemistry*, vol. 2, edited by P. Fritz and J.-C. Fontes, pp. 114–167, Elsevier Sci., Amsterdam.

Hanstrum, B. N., G. A. Mills, A. Watson, J. P. Monteverdi, and C. A. Doswell (2002), The cool season tornadoes of California and southern Australia, *Weather Forecast.*, *17*, 705–723, doi:10.1175/1520-0434(2002)017<0705:TCSTOC>2.0.CO;2.

Helliker, B., and D. Noone (2009), Novel approaches to monitoring of water vapor isotope ratios: Plants, satellites and lasers, in *Isoscapes: Understanding Movement, Pattern, and Process on Earth Through Isotope Mapping*, edited by J. West et al., Springer, New York, in press.

Helsen, M. M., R. S. W. van de Wal, M. R. van den Broeke, V. Masson-Delmotte, H. A. J. Meijer, M. P. Scheele, and M. Werner (2006), Modeling the isotopic composition of Antarctic snow using backward trajectories: Simulation of snow pit records, *J. Geophys. Res.*, *111*, D15109, doi:10.1029/2005JD006524.

Henderson-Sellers, A., K. McGuffie, D. Noone, and P. Irannejad (2004), Using stable water isotopes to evaluate basin-scale simulations of surface water budgets, *J. Hydrometeorol.*, *5*, 805–822, doi:10.1175/1525-7541(2004)005<0805:USWITE>2.0.CO;2.

Hoffmann, G., M. Werner, and M. Heimann (1998), Water isotope module of the ECHAM atmospheric general circulation model: A study on timescales from days to several years, *J. Geophys. Res.*, *103*, 16,871–16,896, doi:10.1029/98JD00423.

Ignaccolo, M., C. De Michele, and S. Bianco (2009), The droplike nature of rain and its invariant statistical properties, *J. Hydrometeorol.*, *10*, 79–95, doi:10.1175/2008JHM975.1.

Jacob, H., and C. Sonntag (1991), An 8-year record of the seasonal variation of ^{2}H and ^{18}O in atmospheric water vapor and precipitation in Heidelberg, Germany, *Tellus, Ser. B*, *43*, 291–300.

Jones, D. A., and I. Simmonds (1993), A climatology of Southern Hemisphere extratropical cyclones, *Clim. Dyn.*, *9*, 131–145, doi:10.1007/BF00209750.

Jones, D. A., and I. Simmonds (1994), A climatology of Southern Hemisphere anticyclones, *Clim. Dyn.*, *10*, 333–348, doi:10.1007/BF00228031.

Joussaume, S., and J. Jouzel (1993), Paleoclimatic tracers: An investigation using an atmospheric general circulation model under ice age conditions: 2. Water isotopes, *J. Geophys. Res.*, *98*, 2807–2830, doi:10.1029/92JD01920.

Joussaume, S., R. Sadourny, and J. Jouzel (1984), A general circulation model of water isotope cycles in the atmosphere, *Nature*, *311*, 24–29, doi:10.1038/311024a0.

Jouzel, J. (1975), Complimentarité des mesures de deutérium et de tritium pour l'étude de la formation de grêlons, *Note CEA N-1833*, 60 pp., Cent. d'Études Nucl. de Saclay, Saclay, France.

Jouzel, J. (1986), Isotopes in cloud physics: Multiphase and multistage condensation processes, in *Handbook of Environmental Isotope Geochemistry*, vol. 2, edited by P. Fritz and J.-C. Fontes, pp. 61–112, Elsevier Sci., Amsterdam.

Jouzel, J., and L. Merlivat (1984), Deuterium and oxygen 18 in precipitation: Modeling of the isotopic effects during snow formation, *J. Geophys. Res.*, *89*, 11,749–11,757, doi:10.1029/JD089iD07p11749.

Jouzel, J., L. Merlivat, and C. Lorius (1982), Deuterium excess in an East Antarctic ice core suggests higher relative humidity at the oceanic surface during the Last Glacial Maximum, *Nature*, *299*, 688–691, doi:10.1038/299688a0.

Jouzel, J., G. L. Russell, R. J. Suozzo, R. D. Koster, J. W. C. White, and W. S. Broeker (1987), Simulations of the HDO and $H_2^{18}O$ atmospheric cycles using the NASA/GISS general circulation model: The seasonal cycle for present day conditions, *J. Geophys. Res.*, *92*, 14,739–14,760, doi:10.1029/JD092iD12p14739.

Jouzel, J., et al. (1997), Validity of the temperature reconstruction from water isotopes in ice cores, *J. Geophys. Res.*, *102*, 26,471–26,488, doi:10.1029/97JC01283.

Kalnay, E., et al. (1996), The NCEP/NCAR reanalysis 40-year project, *Bull. Am. Meteorol. Soc.*, *77*, 437–471, doi:10.1175/1520-0477(1996)077<0437:TNYRP>2.0.CO;2.

Law, R. M. (1993), Modeling the global transport of atmospheric constituents, Ph.D. thesis, Sch. of Earth Sci., Univ. of Melbourne, Melbourne, Victoria, Australia.

Lawrence, J. R., S. D. Gedzelman, J. W. C. White, D. Smiley, and P. Lazov (1982), Storm trajectories in eastern US D/H isotopic composition of precipitation, *Nature*, *296*, 638–664, doi:10.1038/296638a0.

Laws, J. O., and D. A. Parsons (1943), The relation of raindrop size to intensity, *Eos Trans. AGU*, *24*, 452–460.

Lee, J., and I. Fung (2008), "Amount effect" of water isotopes and quantitative analysis of post-condensation processes, *Hydrol. Processes*, *22*, 1–8, doi:10.1002/hyp.6637.

Lee, J., I. Fung, D. J. DePaolo, and C. C. Henning (2007), Analysis of the global distribution of water isotopes using the NCAR atmospheric general circulation model, *J. Geophys. Res.*, *112*, D16306, doi:10.1029/2006JD007657.

Liotta, M., R. Favara, and M. Valenza (2006), Isotopic composition of the precipitations in the central Mediterranean: Origin marks and orographic precipitation effects, *J. Geophys. Res.*, *111*, D19302, doi:10.1029/2005JD006818.

Longinelli, A., and E. Selmo (2003), Isotopic composition of precipitation in Italy: A first overall map, *J. Hydrol.*, *270*, 75–88, doi:10.1016/S0022-1694(02)00281-0.

Lykoudis, S. P., and A. A. Argiriou (2007), Gridded data set of the stable isotopic composition of precipitation over the eastern and central Mediterranean, *J. Geophys. Res.*, *112*, D18107, doi:10.1029/2007JD008472.

Marshall, J. S., and W. M. Palmer (1948), The distribution of raindrops with size, *J. Atmos. Sci.*, *5*, 165–166, doi:10.1175/1520-0469(1948)005<0165:TDORWS>2.0.CO;2.

Martinelli, L. A., R. L. Victoria, L. S. Lobo, S. A. Ribeiro, and M. Z. Moreira (1996), Using stable isotopes to determine sources of evaporated water to the atmosphere in the Amazon basin, *J. Hydrol.*, *183*, 191–204, doi:10.1016/0022-1694(95)02974-5.

Masson-Delmotte, V., J. Jouzel, A. Landais, M. Stievenard, S. J. Johnsen, J. W. C. White, M. Werner, A. Sveinbjornsdottir, and K. Fuhrer (2005), GRIP deuterium excess reveals rapid and orbital-scale changes in Greenland moisture origin, *Science*, *309*, 118–121, doi:10.1126/science.1108575.

Masson-Delmotte, V., et al. (2008), A review of Antarctic surface snow isotopic composition: Observations, atmospheric circulation, and isotopic modeling, *J. Clim.*, *21*, 3359–3387, doi:10.1175/2007JCLI2139.1.

Merlivat, L., and J. Jouzel (1979), Global climatic interpretation of the deuterium-^{18}O relationship for precipitation, *J. Geophys. Res.*, *84*, 5029–5033, doi:10.1029/JC084iC08p05029.

Miyake, Y., O. Matsubaya, and C. Nishihara (1968), An isotopic study on meteoric precipitation, *Pap. Meteorol. Geophys.*, *19*, 243–266.

Noone, D. (2006), Isotopic composition of water vapor modeled by constraining global climate simulations with reanalyses, in *Research Activities in Atmospheric and Oceanic Modeling*, edited by J. Côté, *WMO TD 1347*, pp. 2.37–2.38, World Meteorol. Organ., Geneva, Switzerland.

Noone, D., and I. Simmonds (1999), A three-dimensional spherical trajectory algorithm, in *Research Activities in Atmospheric and Oceanic Modeling*, edited by H. Ritchie, *WMO TD 942*, pp. 3.26–3.27, World Meteorol. Organ., Geneva, Switzerland.

Noone, D., and I. Simmonds (2002), Associations between $\delta^{18}O$ of water and climate parameters in a simulation of atmospheric circulation for 1979–95, *J. Clim.*, *15*, 3150–3169, doi:10.1175/1520-0442(2002)015<3150:ABOOWA>2.0.CO;2.

Noone, D., and C. Sturm (2009), Comprehensive dynamical models of global and regional water isotope distributions, in *Isoscapes: Understanding Movement, Pattern, and Process on Earth Through Isotope Mapping*, edited by J. West et al., Springer, New York, in press.

Peng, H. D., B. Mayer, S. Harris, and H. R. Krouse (2004), A 10-yr record of stable isotope ratios of hydrogen and oxygen in precipitation at Calgary, Alberta, Canada, *Tellus, Ser. B*, *56*, 147–159.

Peng, H. D., B. Mayer, S. Harris, and H. R. Krouse (2007), The influence of below-cloud secondary effects on the stable isotopic composition of hydrogen and oxygen in precipitation at Calgary, Alberta, Canada, *Tellus, Ser. B.*, *59*, 698–704.

Perrin, G., and I. Simmonds (1995), The origin and characteristics of cold-air outbreaks over Melbourne, *Aust. Meteorol. Mag.*, *44*, 41–59.

Pfahl, S., and H. Wernli (2008), Air parcel trajectory analysis of stable isotopes in water vapor in the eastern Mediterranean, *J. Geophys. Res.*, *113*, D20104, doi:10.1029/2008JD009839.

Pionke, H. B., and D. R. DeWalle (1992), Intra- and inter-storm ^{18}O trends for selected rainstorms in Pennsylvania, *J. Hydrol.*, *138*, 131–143, doi:10.1016/0022-1694(92)90160-W.

Rindsberger, M., S. Jaffe, S. Rahamim, and J. R. Gat (1990), Patterns of the isotopic composition of precipitation in time and space: Data from the Israeli storm water collection program, *Tellus, Ser. B.*, *42*, 263–271.

Risi, C., S. Bony, and F. Vimeux (2008), Influence of convective processes on the isotopic composition ($\delta^{18}O$ and δD) of precipitation and water vapor in the tropics: 2. Physical interpretation of the amount effect, *J. Geophys. Res.*, *113*, D19306, doi:10.1029/2008JD009943.

Risi, C., S. Bony, F. Vimeux, M. Chong, and L. Descroix (2009), Evolution of the water stable isotopic composition of the rain sampled along Sahelian squall lines, *Q. J. R. Meteorol. Soc.*, doi:10.1002/qj.485, in press.

Rozanski, K., L. Araguás-Araguás, and R. Gonfiantini (1993), Isotopic patterns in modern global precipitation, in *Climate Change in Continental Isotopic Records*, *Geophys. Monogr. Ser.*, vol. 78, edited by P. K. Swart et al., pp. 1–37, AGU, Washington, D. C.

Salati, E., A. Dall'olio, E. Matsui, and J. R. Gat (1979), Recycling of water in the Amazon basin: An isotopic study, *Water Resour. Res.*, *15*, 1250–1258, doi:10.1029/WR015i005p01250.

Simmonds, I., and K. Keay (2000), Mean Southern Hemisphere extratropical cyclone behavior in the NCEP-NCAR reanalysis, *J. Clim.*, *13*, 873–885, doi:10.1175/1520-0442(2000)013<0873:MSHECB>2.0.CO;2.

Sodemann, H., C. Schwierz, and H. Wernli (2008a), Interannual variability of Greenland winter precipitation sources: 1. Lagrangian moisture diagnostic and North Atlantic Oscillation influence, *J. Geophys. Res.*, *113*, D03107, doi:10.1029/2007JD008503.

Sodemann, H., V. Masson-Delmotte, C. Schwierz, B. M. Vinther, and H. Wernli (2008b), Interannual variability of Greenland winter precipitation sources: 2. Effects of the North Atlantic Oscillation variability on stable isotopes in precipitation, *J. Geophys. Res.*, *113*, D12111, doi:10.1029/2007JD009416.

Stewart, M. K. (1975), Stable isotope fractionation due to evaporation and isotopic exchange of falling water drops: Application to atmospheric processes and evaporation of lakes, *J. Geophys. Res.*, *80*, 1133–1146, doi:10.1029/JC080i009p01133.

Tindall, J. C., P. J. Valdes, and L. C. Sime (2009), Stable water isotopes in HadCM3: Isotopic signature of El Niño–Southern Oscillation and the tropical amount effect, *J. Geophys. Res.*, *114*, D04111, doi:10.1029/2008JD010825.

Vimeux, F., V. Masson, J. Jouzel, M. Stievenard, and J. R. Petit (1999), Glacial-interglacial changes in ocean surface conditions in the Southern Hemisphere, *Nature*, *398*, 410–413, doi:10.1038/18860.

Webster, C. R., and A. J. Heymsfield (2003), Water isotope ratios D/H, $^{18}O/^{16}O$, $^{17}O/^{16}O$ in and out of clouds map dehydration pathways, *Science*, *302*, 1742–1745, doi:10.1126/science.1089496.

Worden, J., et al. (2006), Tropospheric Emission Spectrometer observations of the tropospheric HDO/H_2O ratio: Estimation approach and characterization, *J. Geophys. Res.*, *111*, D16309, doi:10.1029/2005JD006606.

Wright, W. J. (1997), Tropical-extratropical cloudbands and Australian rainfall: 1. Climatology, *Int. J. Climatol.*, *17*, 807–829, doi:10.1002/(SICI)1097-0088(19970630)17:8<807::AID-JOC162>3.0.CO;2-J.

Yoshimura, K., M. Kanamitsu, D. Noone, and T. Oki (2008), Historical isotope simulation using reanalysis atmospheric data, *J. Geophys. Res.*, *113*, D19108, doi:10.1029/2008JD010074.

V. Barras, Centre for Australian Weather and Climate Research, Bureau of Meteorology, 700 Collins St., GPO Box 1289, Melbourne, Vic 3001, Australia. (v.barras@bom.gov.au)

I. Simmonds, School of Earth Sciences, University of Melbourne, Melbourne, Vic 3010, Australia.